

# Mechanisms of Electron Injection from Retinoic Acid and Carotenoic Acids to TiO<sub>2</sub> Nanoparticles and Charge Recombination via the T<sub>1</sub> State As Determined by Subpicosecond to Microsecond Time-Resolved Absorption Spectroscopy: Dependence on the Conjugation Length

Junfeng Xiang, Ferdy S. Rondonuwu, Yoshinori Kakitani, Ritsuko Fujii,<sup>†</sup>  
Yasutaka Watanabe, and Yasushi Koyama\*

*Faculty of Science and Technology, Kwansei Gakuin University, Gakuen, Sanda 669-1337, Japan*

**Hiroyoshi Nagae**

*Kobe City University of Foreign Studies, Gakuen Higashimachi, Nishiku, Kobe 651-2187, Japan*

**Yumiko Yamano and Masayoshi Ito**

*Kobe Pharmaceutical University, Motoyama Kitomachi, Kobe 658-8558, Japan*

*Received: March 22, 2005; In Final Form: June 22, 2005*

To examine the mechanisms of electron injection to TiO<sub>2</sub> in retinoic acid (RA) and carotenoic acids (CAs), including RA5, CA6, CA7, CA8, CA9, and CA11 having the number of conjugated double bonds  $n = 5, 6, 7, 8, 9$ , and  $11$ , respectively, their subpicosecond time-resolved absorption spectra were recorded free in solution and bound to TiO<sub>2</sub> nanoparticles in suspension. The time-resolved spectra were analyzed by singular-value decomposition (SVD) followed by global fitting based on an energy diagram consisting of the  $3A_g^-$ ,  $1B_u^-$ ,  $1B_u^+$ , and  $2A_g^-$  singlet excited states, whose energies had been determined as functions of  $1/(2n + 1)$  by the use of carotenoids with  $n = 9-13$ . It was found that electron injection took place from both the  $1B_u^+$  and  $2A_g^-$  states in RA5, CA6, CA7, and CA8, whereas only from the  $1B_u^+$  state in CA9 and CA11. The electron-injection efficiencies were determined, by the use of the relevant time constants determined by the SVD and global-fitting analyses, to be in the following order: RA5  $\approx$  CA6 < CA7 > CA8 > CA9 > CA11. To determine the mechanism of charge recombination via the T<sub>1</sub> state, submicrosecond time-resolved absorption spectra of RA5, CA6, CA7, and CA8 bound to TiO<sub>2</sub> nanoparticles in suspension were recorded. The SVD and global-fitting analyses lead us to a new scheme, which includes the formation of the  $D_0^{*+} - T_1$  complex followed by transformation to both the  $D_0^{*+}$  and T<sub>1</sub> states. On the other hand, their one-electron oxidation potentials were determined, and their singlet and triplet levels were scaled to the conduction band edge (CBE) of TiO<sub>2</sub>. The T<sub>1</sub> level was lower than, but closest to, the CBE in RA5, and it became lower in the order RA5, CA6, CA7, and CA8. Consistent with the energy gap between the CBE and the T<sub>1</sub> levels, the generation of the T<sub>1</sub> state (or in other words, charge recombination) decreased in the order RA5 > CA6 > CA7 > CA8.

## Introduction

The mechanism of electron injection from a dye to a semiconductor competing with various relaxation processes and subsequent charge recombination through reverse electron transfer from the semiconductor to the dye radical cation is one of the most fundamental issues in understanding the principle of a dye-sensitized solar cell (DSSC) and in enhancing its solar energy-to-electricity conversion efficiency (hereafter, abbreviated as “the conversion efficiency or  $\eta$ ”).

The principles of the Grätzel cell, which now exhibits a conversion efficiency as high as 11.04%, have been most extensively studied.<sup>1–4</sup> The electron-injection mechanisms in the Ru complex–TiO<sub>2</sub> systems have been examined by means of subpicosecond time-resolved absorption spectroscopy: Bi-

exponential electron injection, which includes the first component taking place in the femtosecond time range from the vibrationally hot singlet state (<sup>1</sup>MLCT\*) and the second component taking place in the picosecond time range from the thermalized triplet state (<sup>3</sup>MLCT), was identified.<sup>5–10</sup> The first component competing with vibrational relaxation showed no noticeable variations, whereas the rate and the amount of the second component varied, depending on the sample conditions. The charge recombination took place in the microsecond to millisecond time range.

Recently, DSSCs using organic dyes, which consist of a linear or a ring  $\pi$ -conjugated system and a carboxyl group directly attached to it, have been developed extensively.<sup>11,12</sup> The conversion efficiency has reached a value as high as around 8%.<sup>13</sup> The extent of the  $\pi$ -conjugated system and the peripheral functional groups, inducing its polarization, seem to affect the conversion efficiency. However, systematic studies on the electron-injection and charge-recombination mechanisms have

\* To whom correspondence should be addressed. E-mail: ykoyama@kwansei.ac.jp. Fax: +81-79-565-9077.

<sup>†</sup> Present address: Department of Physics, Graduate School of Science, Osaka City University, Sugimoto, Sumiyoshi-ku, Osaka 558-8585, Japan.

been hampered by the lack of knowledge concerning the excited-state energy levels.

The low-lying singlet and triplet states of carotenoids (Cars) that consist of a linear conjugated chain having approximate  $C_{2h}$  symmetry are now well defined: Most recently, the  $1B_u^-$  and  $3A_g^-$  states have been identified in addition to the well-known  $1B_u^+$  and  $2A_g^-$  states by measurement of resonance-Raman excitation profiles of bacterial Cars.<sup>14–16</sup> Those state energies change as linear functions of  $1/(2n + 1)$ , where  $n$  is the number of conjugated double bonds. The pathways and the time constants of singlet internal conversion and singlet-to-triplet conversion were determined by subpicosecond time-resolved absorption spectroscopy.<sup>17</sup> Further, the detailed mechanisms of Car-to-bacteriochlorophyll (BChl) singlet-energy transfer in the antenna complexes, competing with singlet internal conversion and singlet-to-triplet conversion within Car, have been determined.<sup>18,19</sup> The energetics and the dynamics of the linear  $\pi$ -conjugated systems as well as spectroscopic techniques can now be applied to investigate the mechanisms of electron injection and charge recombination in retinoic acid (RA) and carotenoic acids (CAs), in which a carboxyl group is directly attached to one end of the linear conjugated chain to facilitate the electron-injection and charge-recombination reactions in the  $TiO_2$ –RA and the  $TiO_2$ –CA systems.

Actually, DSSCs consisting of the  $TiO_2$ –CA systems have been developed recently: Kispert and co-workers fabricated a DSSC, for the first time, using CA9 as a sensitizer and hydroquinone as a reductant.<sup>20</sup> It exhibited a reasonably high incident photon to current conversion efficiency (IPCE) of 34% at the absorption maximum at 426 nm, the open-circuit voltage ( $V_{oc}$ ) of 0.15 V, and no bleaching of the dye even after 12 h. We also fabricated DSSCs using RA5, CA6, CA7, CA8, CA9, CA11 and CA13 as the sensitizer and  $I^-/I_3^-$  as the reductant (see the following paper)<sup>21</sup> and determined the conversion efficiency to be 1.0%, 1.2%, 1.5%, 1.2%, 0.9%, 0.3%, and 0.3%, respectively, as shown in the upper panel of Figure 1a. The IPCE values at 420 nm are shown in Figure 1b. The results motivated us to investigate the detailed mechanisms of electron injection and charge recombination.

Concerning the mechanisms, Sundström and co-workers studied the  $TiO_2$ –CA9 system, whereas Weng and co-workers studied the  $TiO_2$ –RA5 system: The former group observed rapid ( $\sim 360$  fs) electron injection from the  $S_2$  ( $1B_u^+$ ) state of CA9 to the conduction band of  $TiO_2$  with a quantum yield of 40%, but no electron injection from the  $S_1$  ( $2A_g^-$ ) state.<sup>22</sup> They observed charge recombination in the picosecond to microsecond time range between the injected electron on  $TiO_2$  and the dye radical cation  $CA9^{+\bullet}$ : approximately one-half to generate the ground state and the other half to generate the  $T_1$  state. On the other hand, the latter group first proposed charge recombination between  $TiO_2^-$  and  $RA5^{+\bullet}$  to generate the  $T_1$  state.<sup>23</sup> Further, Zhang et al. showed electron injection from both the  $1B_u^+$  and  $n\pi^*$  states of RA5 to  $TiO_2$ , and charge recombination to generate mainly the  $T_1$  state.<sup>24</sup>

Inspired by those pioneering works, we have examined the conjugation-length ( $n$ ) dependence of the mechanisms of electron injection and charge recombination in RA5, CA6, CA7, CA8, CA9, and CA11 bound to  $TiO_2$  nanoparticles. We have addressed the following three specific questions: (1) How do the electron-injection pathway and efficiency depend on  $n$ ? (2) How does the charge recombination via the  $T_1$  state depend on  $n$ ? (3) How do those dependencies on  $n$  correlate with those of

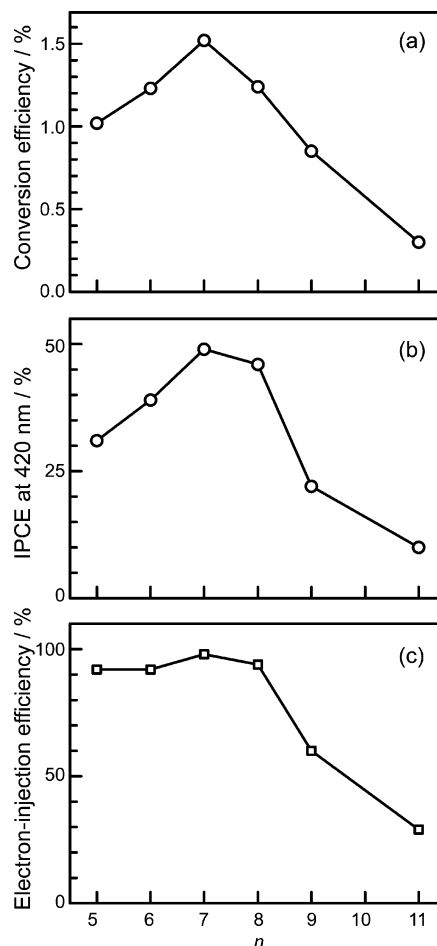


**Figure 1.** Dependence on  $n$  of (a) the conversion efficiency,  $\eta$ , and (b) the IPCE at 420 nm in DSSCs using RA or CAs bound to the  $TiO_2$  layer and (c) the efficiency of electron injection from RA or CA to  $TiO_2$  nanoparticles in suspension.

the conversion efficiency and the IPCE when DSSCs are fabricated by the use of the  $TiO_2$ –RA and the  $TiO_2$ –CA systems?

## Experimental Section

**Sample Preparation.** (a) *Preparation of RA5 and CAs.* *all-trans*-Retinoic acid (RA5) was used as received from Sigma.  $\beta$ -Apo-14'-carotenoic acid (CA6),  $\beta$ -apo-12'-carotenoic acid (CA7), and  $\beta$ -apo-10'-carotenoic acid (CA8) were prepared as described in the following paper.<sup>21</sup>  $\beta$ -Apo-8'-carotenoic acid (CA9) and  $\beta$ -apo-4'-carotenoic acid (CA11) were also obtained by hydrolysis of their ethyl esters, which were gifts from Dr. Hansgeorg Ernst, BASF. The purities of RA and CAs were determined by HPLC, using the detection wavelength at 365 nm for RA5 and at 450 nm for CA6–CA11, to be RA5–CA8 100%, CA9 99%, and CA11 96%.

(b) *Preparation of  $TiO_2$  Particles.* A 8.0 g/L colloidal solution of  $TiO_2$  was prepared by hydrolysis of titanium isopropoxide (special grade, Wako Chemicals, Japan) at  $\sim 0^\circ C$  in acidified ethanol (pH  $\sim 2$ ).<sup>23</sup> The  $TiO_2$  solution was diluted by about 10 times, and then RA or CA was added to a concentration as specified below. The molar ratio of RA(CAs): $TiO_2$  was on the order of 1:100.

**Time-Resolved Electronic Absorption Spectroscopies.** (a) *Subpicosecond Time-Resolved Absorption Spectroscopy.* The experimental setup was described previously.<sup>25,26</sup> Each RA or CA was first dissolved in a small amount of tetrahydrofuran

(THF), and then diluted with ethanol (both solvents were spectroscopic grade, Wako Chemicals, Japan). The concentration of each RA or CA solution, without or with TiO<sub>2</sub>, was adjusted to OD =  $\sim 5$  cm<sup>-1</sup>, while in RA5, to OD =  $\sim 8$  cm<sup>-1</sup> at the absorption maximum ( $\lambda_{\text{max}}$ ). For each measurement, a 25–30 mL sample solution was circulated between a 1 mm flow cell and a reservoir cooled in ice–water (no degassing with nitrogen was done).

The wavelength of excitation was 400, 400, 426, 445, 460, and 496 nm for RA5, CA6, CA7, CA8, CA9, and CA11 free in solution, while 400, 400, 436, 455, 470, and 510 nm when bound to TiO<sub>2</sub> nanoparticles in suspension. The repetition rate, the pulse duration, and the power of the pumping pulses were 1 kHz, 130 fs, and  $\sim 0.5$   $\mu$ J/pulse, respectively. White-continuum probing pulses, in the visible and near-infrared regions, were generated by irradiating a 1 cm water flow cell and a 0.5 cm sapphire plate, respectively.

The time-resolved spectral data at each delay time were accumulated for  $3 \times 300$  pulses. The data matrixes of RA5, CA6, CA7, and CA8, which were used for singular-value decomposition (SVD) followed by global fitting,<sup>27</sup> had a dimension of 1105 data points in the 400–800 nm spectral region, and 300 data points in the –2 to 50 ps time region for RA5, CA6, CA7, and CA8, while those of CA9 and CA11 had a dimension of 1105 data points in the 820–1020 nm region and 260 data points in the –2 to 20 ps region.

*(b) Submicrosecond Time-Resolved Absorption Spectroscopy.* The experimental setup was described previously.<sup>28</sup> In the determination of the  $T_n \leftarrow T_1$  absorption of RA and CAs free in solution, anthracene (Special grade, Wako Chemicals, Japan) was used as a sensitizer for triplet excitation. The molar ratio of sensitizer vs RA or CA was set to be  $\sim 20$ , and the overall concentration was adjusted to OD =  $\sim 3.5$  cm<sup>-1</sup> at 355 nm. Before each measurement, the sample solution was degassed with high-purity nitrogen gas for at least 1 h. The sample solution was continuously purged with nitrogen gas, when it was circulated between a 2 mm flow cell and a 25 mL reservoir. At each delay time, the spectral data were accumulated for 20 pulses.

The excited-state dynamics in the submicrosecond to hundred microsecond region were also examined for RA5, CA6, CA7, and CA8 bound to TiO<sub>2</sub> nanoparticles in suspension. The concentrations of the sample solutions were adjusted to OD =  $\sim 5$  cm<sup>-1</sup> at the excitation wavelengths, which were the same as subpicosecond time-resolved absorption spectroscopy. Each sample solution was bubbled with argon gas for 1.5 h before measurement under the argon atmosphere at room temperature. The pump pulses (duration 10 ns, power 1 mJ/pulse, and repetition 2 Hz) were generated by a dye laser seeded by the TH 355 nm pulses from a Nd:YAG laser. Dyes used include Exalite 398 for generating the 400 nm pulses and Coumarin 2 for generating the 436 and 455 nm pulses. At each delay time, the spectral data were accumulated for 20 pulses in the visible region and 40 pulses in the near-infrared region. The spectral data matrixes of RA5, CA6, CA7, and CA8, which were used in the SVD and global fitting analyses, had a dimension of 453, 538, 704, and 750 data points in the 380–650, 380–700, 380–800, and 380–830 nm spectral regions, respectively; all the data matrixes had a dimension of 70 data points in the –2 to 90  $\mu$ s time region.

*(c) Relevant Parameters Concerning Time-Resolved Absorption Spectroscopy.* The photon density of each laser pulse in the present subpicosecond (microsecond) time-resolved absorption spectroscopy was  $3.7 \times 10^{13}$  ( $5.4 \times 10^{16}$ )

photon·cm<sup>-2</sup>·pulse<sup>-1</sup>. Assuming that the molar extinction coefficient of CA7 is the same as that of  $\beta$ -apo-12'-carotenal, i.e.,  $\epsilon = 75\,600$  M<sup>-1</sup> cm<sup>-1</sup>,<sup>29</sup> the number of molecules in the laser beam in the cell was  $1.9 \times 10^{14}$  ( $3.2 \times 10^{14}$ ) molecules in the case of subpicosecond (submicrosecond) time-resolved absorption spectroscopy, whereas the number of photons traveling through the beam was  $1.1 \times 10^{12}$  ( $2.2 \times 10^{15}$ ) photon pulse<sup>-1</sup>. The number of photons absorbed was  $9.2 \times 10^{11}$  ( $2.0 \times 10^{15}$ ) photon pulse<sup>-1</sup>, and therefore, the ratio of the number of photons absorbed vs the number of molecules irradiated became  $4.8 \times 10^{-3}$  (6.3) photon·molecule<sup>-1</sup>. Therefore, there is little chance of multiphoton excitation in subpicosecond time-resolved absorption spectroscopy, but there is a good chance of multiphoton excitation in submicrosecond time-resolved absorption spectroscopy.

Under the *latter* conditions, it is known that charge recombination becomes faster,<sup>30</sup> and electron injection efficiency is reduced.<sup>31</sup>

Assuming the diffusion coefficient ( $D$ ) of CA at room temperature to be  $\sim 10^{-6}$  cm<sup>2</sup> s<sup>-1</sup>, the average distance of diffusion within the pulse duration can be calculated, by the use of the equation  $\langle x^2 \rangle = 2Dt$ , to be 0.03 Å (10 Å) in the subpicosecond (submicrosecond) time-resolved absorption spectroscopy. On the other hand, the average molecule-to-molecule distance in solution, at the present concentration, is estimated to be 250 (290) Å. Therefore, there is no chance of collisions among the excited-state molecules during the pulse duration.

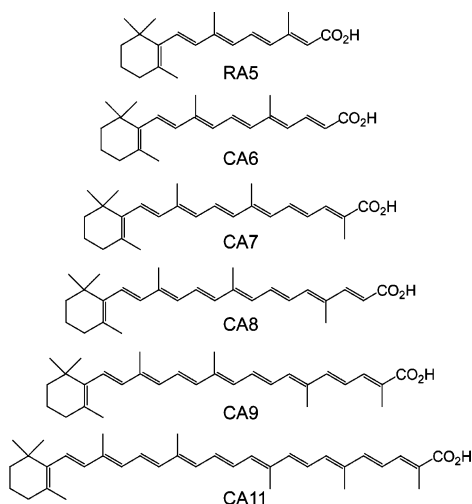
**Electrochemical and Spectroelectrochemical Measurements.** *(a) Cyclic Voltammetry.* The solvent, dichloromethane (spectroscopic grade, Wako Chemicals, Japan), was purified by passing through an alumina column (Merck, Aluminum Oxide 90, activity II–III), and stored with a 3 Å molecular sieve (Kishida Chemicals, Japan) before use. The supporting electrolyte, tetrabutylammonium hexafluorophosphate (TBAHFP, polarographic grade, Sigma), was used without further purification. The concentration of TBAHFP was  $\sim 0.1$  M and those of RA and CAs were in the region of  $10^{-3}$ – $10^{-4}$  M (the  $\epsilon$  values have not been determined). The solution was degassed with nitrogen before each measurement.

Cyclic voltammetry was carried out by the use of a potentiostat (HA1010mM1A, Hokuto Denko, Japan). The working and counter electrodes were a platinum wire (0.5 mm in diameter), and the reference electrode was a Ag/AgCl electrode. The scan rate was 100 mV/s.

*(b) Spectroelectrochemical Measurements.* The sample conditions were described above. The electronic-absorption spectrum of each sample solution, at a specified redox potential, was measured by the use of a Hitachi U-2000 spectrophotometer and a spectroelectrochemical cell built as a collaboration with Hokuto Denko. The cell consisted of a pair of quartz plates and a Teflon spacer (0.3 mm thick). The working electrode (100 mesh platinum gauze) and the reference electrode (platinum foil) were coated on one of the quartz plates, while the counter electrode (platinum foil) was coated on the other plate, by the use of a screen-coating technique; the thickness of the gauze and the platinum foil was about several micrometers. The counter electrode (platinum foil) has a square hole in the center, and was aligned facing against the working electrode (gauze) so that the probe light could pass through the gauze. The above components were assembled in a 1 cm optical cell to set into the sample holder in the spectrophotometer. A spectrum of the spectroelectrochemical cell recorded with no sample solution was used as the reference for the background subtraction.



## SCHEME 1: Chemical Structures of RA and CAs

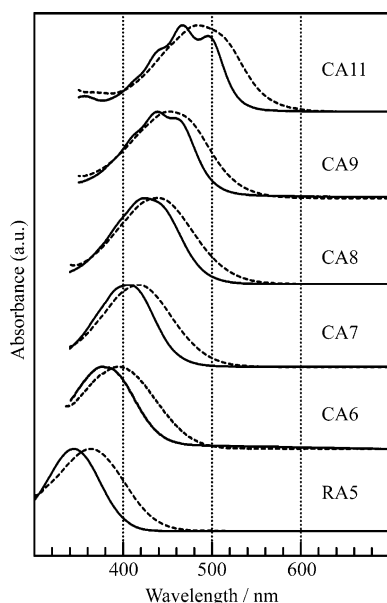


## Results

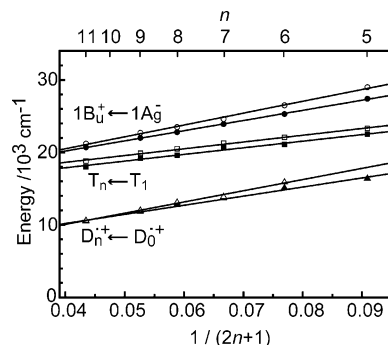
## Characterization of Retinoic Acid and Carotenoid Acids.

(1) *Chemical Structures and the Effects of Binding to  $\text{TiO}_2$ .* Scheme 1 shows the chemical structures of RA and CAs used in the present investigation. They are named according to the number of conjugated double bonds ( $n$ ). In all the RA and CAs, the  $\beta$ -ionone ring is attached to the one end, and the carboxyl group to the other end of the conjugated chain. CAs having different lengths of conjugated chain are the derivatives of  $\beta$ -carotene, and therefore the positions of the methyl groups originate from those in the parent molecule. Some of their photophysical and photochemical properties are expected to systematically change depending on  $n$ .

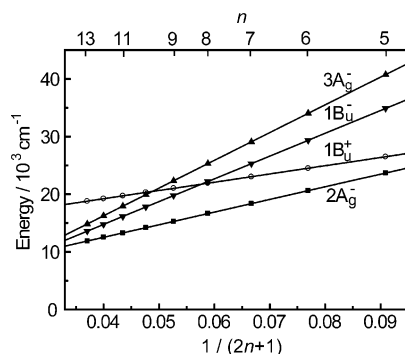
Figure 2 shows the electronic absorption spectra of RA and CAs free in ethanol solution and those bound to  $\text{TiO}_2$  nanoparticles in suspension. [Table A in the Supporting Information lists the wavelengths (the energies) of the  $1\text{B}_u^+ \leftarrow 1\text{A}_g^-$  (the ground state),  $\text{T}_n \leftarrow \text{T}_1$  (the lowest triplet state), and  $\text{D}_n^{\bullet+} \leftarrow \text{D}_0^{\bullet+}$  (the radical cation state) absorptions for the set of RA and



**Figure 2.** Electronic absorption spectra of RA and CAs free in ethanol solution (solid lines) and bound to  $\text{TiO}_2$  nanoparticles in suspension (broken lines). The absorption spectra of RA and CAs bound to  $\text{TiO}_2$  nanoparticles in suspension were recorded by the use of  $\text{TiO}_2$  solution as the reference.



**Figure 3.** The energies of the  $1\text{B}_u^+ \leftarrow 1\text{A}_g^-$ ,  $\text{T}_n \leftarrow \text{T}_1$  and  $\text{D}_n^{\bullet+} \leftarrow \text{D}_0^{\bullet+}$  absorptions in RA and CAs free in ethanol solution (open circles, open squares, and open triangles) and bound to  $\text{TiO}_2$  nanoparticles in ethanol suspension (closed circles, closed squares, and closed triangles).

SCHEME 2: Energy Diagram for RA and CAs Obtained by Extrapolation of the Singlet-State Energies of Cars ( $n = 9\text{--}13$ ) as Linear Functions of  $1/(2n + 1)$ 

CAs free in solution and bound to  $\text{TiO}_2$  nanoparticles; the shifts of the absorption bands upon binding to  $\text{TiO}_2$  ( $\Delta$ ) are also shown.] Figure 3 shows the energies of all three different transitions that change as linear functions of  $1/(2n + 1)$ . The effects of binding to  $\text{TiO}_2$  can be characterized as follows: (1) The  $1\text{B}_u^+ \leftarrow 1\text{A}_g^-$  absorption shifts to the lower energies (open to closed circles); the amount of shift is the largest in the RA5, and systematically decreases when  $n$  increases. (2) The  $\text{T}_n \leftarrow \text{T}_1$  absorption also shifts to the lower energy (open to closed squares); the amounts of shift are more or less similar irrespective of  $n$ . (3) The  $\text{D}_n^{\bullet+} \leftarrow \text{D}_0^{\bullet+}$  absorption may exhibit the largest shift in RA5 (the absorption for free RA5 could not be recorded spectroelectrochemically), and then, the amount of shift decreases systematically where  $n$  increases (open to closed triangles). (4) In both the  $1\text{B}_u^+ \leftarrow 1\text{A}_g^-$  and the  $\text{D}_n^{\bullet+} \leftarrow \text{D}_0^{\bullet+}$  absorptions, the effects of binding to  $\text{TiO}_2$  are larger in RA or CAs having a shorter conjugated chain than CAs having a longer conjugated chain. The results suggest that the effects of binding, i.e., withdrawal of electron through the terminal carboxyl group, are suppressed by a large number of delocalized  $\pi$  electrons in the longer conjugated chain (the buffering effect).

(2) *The State Energies and the Internal-Conversion Processes Expected for the Series of RA and CAs.* Scheme 2 shows an energy diagram that we propose for RA and CAs with  $n = 5\text{--}13$ . It is based on the extrapolation, toward smaller  $n$ , of the state energies in bacterial carotenoids ( $n = 9\text{--}13$ ) that were determined by measurement of resonance-Raman excitation profiles.<sup>16</sup> The slopes of the linear relations as functions of  $1/(2n + 1)$  were in the ratio, i.e.,  $2\text{A}_g^-:1\text{B}_u^-:3\text{A}_g^- = 2:3.1:3.8$ , which were in excellent agreement with that calculated for shorter polyenes with  $n = 5\text{--}8$ , i.e.,  $2\text{A}_g^-:1\text{B}_u^-:3\text{A}_g^- = 2:3.1:3.7$ .<sup>32</sup> This agreement was actually the basis for the assignment of those states. According to the selection rule using Pariser's signs,

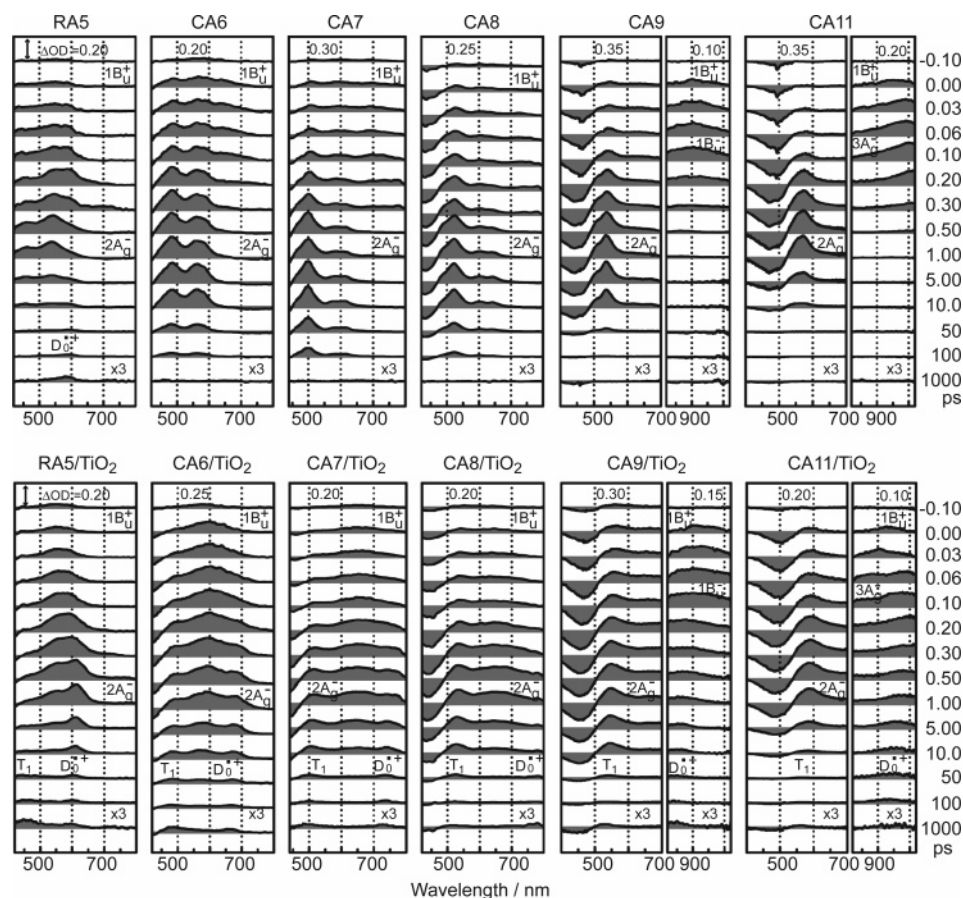


**Figure 4.** Subpicosecond time-resolved absorption spectra of RA and CAs free in ethanol solution (the upper panels) and bound to  $\text{TiO}_2$  nanoparticles in ethanol suspension (the lower panels). The ordinate scales of time-resolved spectra at 1 ns are expanded by 3 times.

+ and  $-$ ,<sup>33</sup> electronic transition accompanying absorption or emission of photon is allowed between a pair of singlet states having different signs, whereas internal conversion is allowed between a pair of states having the same sign.<sup>34</sup> However, the latter selection rule does not hold strictly when a pair of states is located close-by.<sup>15</sup> Thus, the CA molecule can be excited, by absorption of photon, from the ground  $1A_g^-$  state to the  $1B_u^+$  state. Then, the next-lower singlet state to internally convert is the  $2A_g^-$  state in RA5–CA8, the  $1B_u^-$  state in CA9, and the  $3A_g^-$  state in CA11. Further internal conversion should follow according to the state ordering. In addition, it should be remembered that the  $D_0^{*+}$  state can be generated as the result of electron injection from RA or CAs to  $\text{TiO}_2$ , and that the ground ( $1A_g^-$ ) or the  $T_1$  state can be generated, in general, through the reverse electron transfer followed by charge recombination.

**Electron-Injection Mechanisms in the Subpicosecond to Picosecond Time Region.** (1) *Empirical Characterization of Subpicosecond Time-Resolved Spectra.* Figure 4 shows the time-resolved absorption spectra of RA5, CA6, CA7, CA8, CA9, and CA11 free in ethanol solution (the upper panels) and bound to  $\text{TiO}_2$  nanoparticles in ethanol suspension (the lower panels). (a) *RA and CAs Free in Solution (the upper panels).* In RA5–CA8, transient absorptions accompanying the vibrational progression on the longer-wavelength side appear immediately after photoexcitation. It can be definitely assigned to the  $1B_u^+$  state, to which all those molecules were excited. The other spectral features appearing around 1 ps can be assigned to the  $2A_g^-$  state according to the state ordering shown in Scheme 2.

In CA9 and CA11, similar spectral changes ascribable to the transformations from the  $1B_u^+$  state eventually to the  $2A_g^-$  state

are not clearly seen in the visible region (400–700 nm). In the near-infrared region (820–1020 nm), a transient absorption ascribable to the  $1B_u^-$  state is seen in CA9, whereas another transient absorption ascribable to the  $3A_g^-$  state is seen in CA11, temporally between the  $1B_u^+$  and the  $2A_g^-$  states. Transient absorptions similar to the above were observed in the case of nonpolar Cars, neurosporene ( $n = 9$ ) and lycopene ( $n = 11$ ).<sup>26</sup>

(b) *RA and CAs Bound to  $\text{TiO}_2$  in Suspension (the lower panels).* In RA5–CA8, broad transient absorptions appear immediately after excitation, which can be assigned to the  $1B_u^+$  state. After 1 ps, transient absorptions that are shifted to the red appear; they can be assigned to the  $2A_g^-$  state according to the state ordering. At 50 ps, the  $T_n \leftarrow T_1$  and the  $D_n^{*+} \leftarrow D_0^{*+}$  absorptions appear on the shorter and longer wavelength side of the  $2A_g^-$  transient absorption (hereafter, abbreviated as “the  $T_1$  and  $D_0^{*+}$  absorptions”, respectively). The bases for the assignment of those two transient absorptions will be given in the next section.

In neither CA9 nor CA11 is the transient absorptions in the visible region presumably originating from the  $1B_u^+ \rightarrow 2A_g^- \rightarrow T_1$  electronic conversion clearly time-resolved, although small time-dependent spectral shifts to the shorter wavelength region, which is ascribable to the  $2A_g^- \rightarrow T_1$  conversion, are seen. In the near-infrared region, however, spectral changes showing the transformations of  $1B_u^+ \rightarrow 1B_u^- \rightarrow D_0^{*+}$  can be recognized in CA9, whereas those showing the transformations of  $1B_u^+ \rightarrow 3A_g^- \rightarrow D_0^{*+}$  can be recognized in CA11.

(2) *Singular-Value Decomposition and Global-Fitting Analysis of Time-Resolved Spectra.* (a) *Species-Associated Difference Spectra (SADS).* Figure 5 shows the SADS of RA and CAs free in solution (the upper panels) and bound to  $\text{TiO}_2$  nanopar-

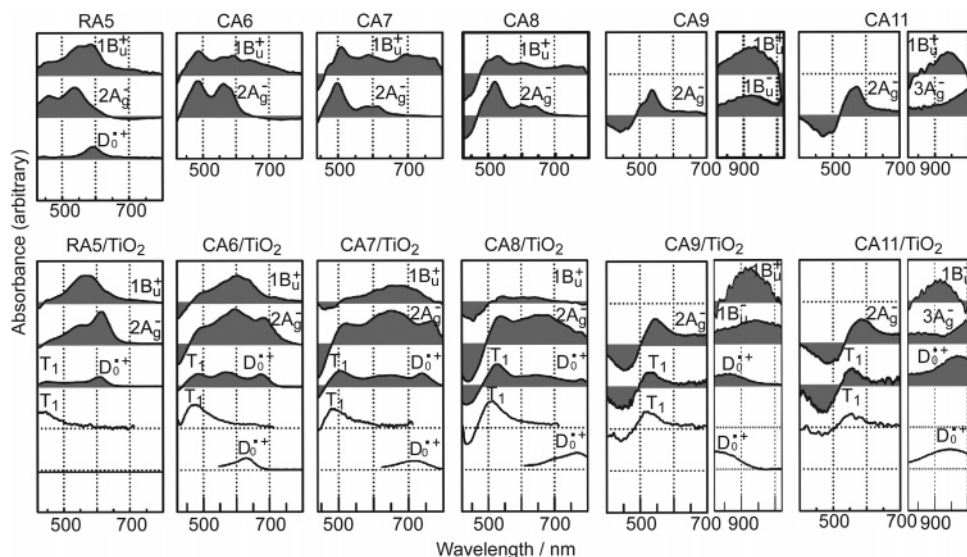


**Figure 5.** The results of the SVD and global-fitting analyses of subpicosecond time-resolved absorption spectra for RA and CAs free in solution (the upper panels) and bound to TiO<sub>2</sub> nanoparticles in suspension (the lower panels): A set of SADS (see also Figure 6). In the lower panels, the spectra of the T<sub>1</sub> and D<sub>0</sub><sup>+</sup> states, for free RA and CAs, generated by triplet-sensitized excitation and by one-electron oxidation are shown for comparison.

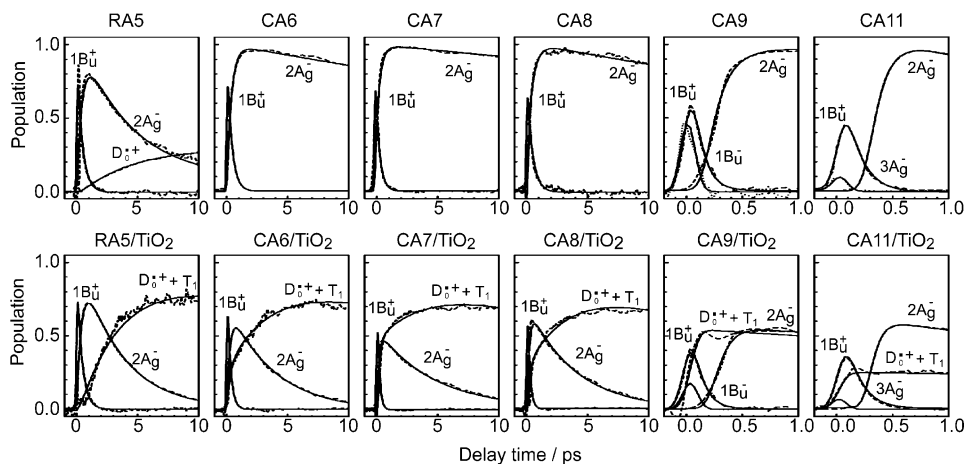


**Figure 6.** A set of time-dependent changes in population (see the caption of Figure 5).

ticles in suspension (the lower panels). The typical spectral pattern of each electronic state is now clearly extracted as SADS by the SVD and global-fitting analyses (the details of the models used will be described in Section c below): In RA5–CA8, the SADS of transient absorptions from the 1B<sub>u</sub><sup>+</sup> and 2A<sub>g</sub><sup>−</sup> states exhibit different relative intensities of their vibrational structures, either free in solution or bound to TiO<sub>2</sub> nanoparticles, a fact which suggests that the shifts of the potential minima upon  $m\text{A}_g^- \leftarrow 1\text{B}_u^+$  and  $n\text{B}_u^+ \leftarrow 2\text{A}_g^-$  electronic transitions (the Franck–Condon factor) may vary from one RA or CA to another depending on  $n$ . The SADS of the long-standing components in the TiO<sub>2</sub>–RA and TiO<sub>2</sub>–CA adducts can be ascribed to a mixture of the T<sub>1</sub> and D<sub>0</sub><sup>+</sup> absorptions, on the basis of spectral comparison with the T<sub>1</sub> states of free RA and CAs that were generated by anthracene-sensitized excitation and spectral comparison with the D<sub>0</sub><sup>+</sup> states of free CAs that were generated electrochemically (see the spectral lines at the bottom part of the lower panels). Both the T<sub>1</sub> and D<sub>0</sub><sup>+</sup> transient absorptions of CAs bound to TiO<sub>2</sub> are shifted to the red in comparison to those free in solution (see Figure 3 and Table A in the Supporting Information).

In CA9 and CA11, subtle time-dependent changes in the visible region did not allow us to perform the SVD and global-

fitting analyses; therefore, raw time-resolved spectra, in which the contributions of the 2A<sub>g</sub><sup>−</sup> and the T<sub>1</sub> absorptions seem to be at the maxima, are presented. In the near-infrared region, the assignment of the 1B<sub>u</sub><sup>+</sup> and 3A<sub>g</sub><sup>−</sup> transient absorptions is confirmed by spectral comparison with neurosporene and lycopene (see Figure 4 of ref 26). Here again, the assignment of the T<sub>1</sub> and D<sub>0</sub><sup>+</sup> transient absorptions for CAs bound to TiO<sub>2</sub> was given by spectral comparison with the T<sub>1</sub> and D<sub>0</sub><sup>+</sup> absorptions for CAs free in solution, which were generated by sensitized excitation and electrochemical oxidation, respectively.

At this moment, it is not completely clear that the last component seen in RA and CAs bound to TiO<sub>2</sub>, which exhibits both the T<sub>1</sub> and D<sub>0</sub><sup>+</sup> absorptions, is either due to a mixture of the D<sub>0</sub><sup>+</sup> and T<sub>1</sub> states or due to the D<sub>0</sub><sup>+</sup>–T<sub>1</sub> complex (vide infra). Until the situation becomes clear, we will use the words “the D<sub>0</sub><sup>+</sup>(T<sub>1</sub>) absorption” instead of “the D<sub>0</sub><sup>+</sup>(T<sub>1</sub>) state” in the text, and indicate as “D<sub>0</sub><sup>+</sup> + T<sub>1</sub>” in Figure 6.

(b) *Time-Dependent Changes in Population.* Figure 6 shows the time-dependent changes in population on the relevant electronic states, in RA and CAs free in solution and bound to TiO<sub>2</sub> nanoparticles. In RA5, the 1B<sub>u</sub><sup>+</sup> state rapidly transforms into the 2A<sub>g</sub><sup>−</sup> state, which decays quickly either free in solution or bound to TiO<sub>2</sub>. A certain amount of the D<sub>0</sub><sup>+</sup> absorption is



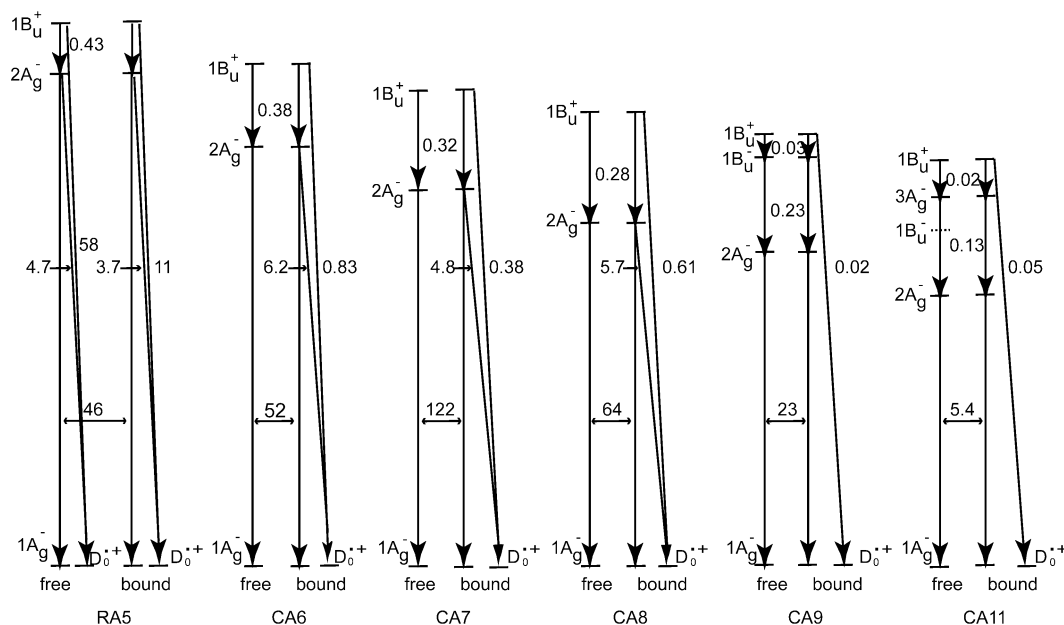


**Figure 7.** The pathways of internal conversion and electron injection for RA and CAs free in solution and bound to TiO<sub>2</sub> nanoparticles in suspension. The time constant for each pathway is shown in picoseconds.

seen even free in solution, whereas a large amount of the D<sub>0</sub><sup>++</sup> and T<sub>1</sub> absorptions is seen when bound to TiO<sub>2</sub>. In CA6, CA7, and CA8, the time profiles of the excited-state population are similar to one another: When free in solution, the 2A<sub>g</sub><sup>-</sup> state is generated in a large amount and decays slowly, whereas when bound to TiO<sub>2</sub>, the D<sub>0</sub><sup>++</sup> and T<sub>1</sub> absorptions are generated efficiently from both the 1B<sub>u</sub><sup>+</sup> and 2A<sub>g</sub><sup>-</sup> states. In CA9, a sequential internal conversion of 1B<sub>u</sub><sup>+</sup> → 1B<sub>u</sub><sup>-</sup> → 2A<sub>g</sub><sup>-</sup> is seen, whereas in CA11, that of 1B<sub>u</sub><sup>+</sup> → 3A<sub>g</sub><sup>-</sup> → 2A<sub>g</sub><sup>-</sup> is either free in solution or bound to TiO<sub>2</sub> nanoparticles. When bound to TiO<sub>2</sub>, the D<sub>0</sub><sup>++</sup> + T<sub>1</sub> signal appear and stay at the longer delay times.

(c) *Electron-Injection Mechanisms and Efficiencies.* Figure 7 shows all the electronic conversion pathways and the relevant time constants in RA and CAs, free in solution and bound to TiO<sub>2</sub> nanoparticles, which have been determined by the SVD and global-fitting analyses. In the analyses of RA and CAs bound to TiO<sub>2</sub>, the time constants of internal conversion that had been determined free in solution were directly transferred, and changes in the excited state dynamics were solely ascribed to the electron-injection reaction(s). Most importantly, the global-fitting analyses lead us to a conclusion that RA5, CA6, CA7, and CA8 have two channels of electron injection from both the 1B<sub>u</sub><sup>+</sup> and 2A<sub>g</sub><sup>-</sup> states, whereas CA9 and CA11 have only one channel from the 1B<sub>u</sub><sup>+</sup> state.

The internal-conversion dynamics in RA and CAs, both free and bound, can be characterized as follows: (1) The lifetime of the 2A<sub>g</sub><sup>-</sup> state is systematically shortened on going from CA7 to CA11, when the 2A<sub>g</sub><sup>-</sup> → 1A<sub>g</sub><sup>-</sup> energy gap decreases, in accord with the energy-gap law.<sup>35</sup> (2) On the other hand, the 2A<sub>g</sub><sup>-</sup> lifetime becomes substantially shortened on going from CA7 to RA5 even though the energy gap becomes larger. (3) The time constant of the 1B<sub>u</sub><sup>+</sup> → 2A<sub>g</sub><sup>-</sup> conversion becomes systematically shortened on going from RA5 to CA8, although the 1B<sub>u</sub><sup>+</sup> → 2A<sub>g</sub><sup>-</sup> energy gap increases. Obviously, the latter two cases, (2) and (3), are against the energy-gap law. Those results contradict the cases of nonpolar bacterial carotenoids having *n* = 9–13, where the 1B<sub>u</sub><sup>+</sup> and 2A<sub>g</sub><sup>-</sup> lifetimes follow the energy-gap law.<sup>26,36</sup> The above case (2) can be explained in terms of electronic mixing between the 2A<sub>g</sub><sup>-</sup> and the 1B<sub>u</sub><sup>+</sup> states. As a result of mixing, the covalent 2A<sub>g</sub><sup>-</sup> state must obtain some ionic character to enhance the radiative transition down to the 1A<sub>g</sub><sup>-</sup>

**TABLE 1: Electron-Injection Efficiencies (in %) through the 1B<sub>u</sub><sup>+</sup> and the 2A<sub>g</sub><sup>-</sup> Channels and a Sum of Them Calculated by the Use of Time Constants Shown in Figure 4**

|                                      | RA5  | CA6  | CA7  | CA8  | CA9  | CA11 |
|--------------------------------------|------|------|------|------|------|------|
| 1B <sub>u</sub> <sup>+</sup> channel | 0.04 | 0.31 | 0.46 | 0.31 | 0.60 | 0.29 |
| 2A <sub>g</sub> <sup>-</sup> channel | 0.88 | 0.61 | 0.52 | 0.63 |      |      |
| total                                | 0.92 | 0.92 | 0.98 | 0.94 | 0.60 | 0.29 |

state. Since the 1B<sub>u</sub><sup>+</sup> → 2A<sub>g</sub><sup>-</sup> energy gap decreases on going from CA7 to RA5, the electronic mixing and, as a result, the radiative transition must be enhanced in this order. The stimulated emission above 650 nm that is seen in the SADS of RA5 and CA6 (see Figure 5) supports this interpretation. Case (3) can be explained in terms of the withdrawal of the π-electron from the conjugated system by the terminal carboxyl group, which will enhance the ionic character of the 1B<sub>u</sub><sup>+</sup> state and, as a result, radiative transition to the ground state. The effect should be stronger in RA5 and CA6 having a shorter conjugated chain, because the π-electrons in a longer conjugated chain can function as a buffer. The shift of the 1B<sub>u</sub><sup>+</sup> ← 1A<sub>g</sub><sup>-</sup> absorption upon binding to TiO<sub>2</sub> nanoparticles is larger in shorter chain RA and CAs (see Figure 3), an observation which supports this idea that the π-electrons function as a buffer. (4) One of the reviewers asked us why the electron-injection from the 1B<sub>u</sub><sup>+</sup> state slows down on going from CA7 to RA5. A possible answer to this question is as follows: The electronic mixing between the 1B<sub>u</sub><sup>+</sup> and 2A<sub>g</sub><sup>-</sup> states is expected to be enhanced when the energy gap between those states is decreased. Further, electronic injection from the ionic 1B<sub>u</sub><sup>+</sup> state should be more efficient than that from the covalent 2A<sub>g</sub><sup>-</sup> state. Then, on going from *n* = 7 to *n* = 5, the 1B<sub>u</sub><sup>+</sup> state must gain more 2A<sub>g</sub><sup>-</sup> character, and then electron injection from this state should become suppressed.

Table 1 lists the electron-injection efficiencies, through both the 1B<sub>u</sub><sup>+</sup> and 2A<sub>g</sub><sup>-</sup> channels, that were calculated for the set of RA and CAs by the use of the relevant time constants shown in Figure 7. The total electron-injection efficiencies are depicted in Figure 1c. Thus, the highest electron-injection efficiency is achieved for the conjugation length with *n* = 7, as in the case of the conversion efficiency (Figure 1a) and the incident photon to current conversion efficiency (IPCE) at 420 nm (Figure 1b)

**TABLE 2: One-Electron Oxidation Potentials in Dichloromethane (in V)**

|                              | RA5  | CA6  | CA7  | CA8  | CA9  | CA11 |
|------------------------------|------|------|------|------|------|------|
| $E_{\text{ox}}$ (vs Ag/AgCl) | 1.08 | 0.97 | 0.87 | 0.80 | 0.77 | 0.71 |

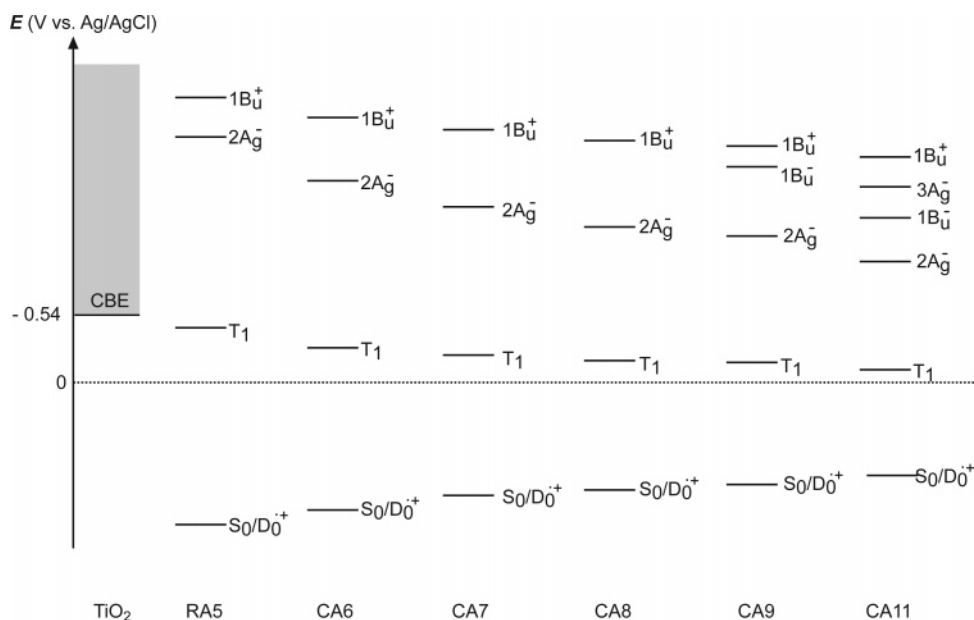
when the DSSCs were fabricated. Obviously, the electron-injection efficiency is one of the most important factors to determine the IPCE and, as a result, the conversion efficiency.

**Charge Recombination Mechanisms in the Microsecond Time Region.** (1) *Cyclic Voltammetry and the Scaling of the Excited-State Energies of RA and CAs to That of the Conduction Band-Edge (CBE) of  $\text{TiO}_2$ .* Table 2 lists the values of one-electron oxidation potential in dichloromethane that were determined by cyclic voltammetry for the set of RA and CAs in reference to the Ag/AgCl electrode. Scheme 3 shows the results of scaling of the singlet and triplet levels of RA and CAs to the CBE of  $\text{TiO}_2$  by the use of the one-electron oxidation potentials ( $S_0/D_0^{+}$ ) of RA and CAs. The  $T_1$  energy of each RA or CA is assumed to be one-half of the  $2A_g^-$  energy,<sup>37</sup> an assumption that has been shown to be the case in Cars with  $n = 9-11$  bound to the LH2 complexes from purple photosynthetic bacteria.<sup>38</sup> The energy of the CBE was calculated from the relation  $E_{\text{CBE}} = -0.1 - 0.059\text{pH}$  (in V) vs NHE,<sup>39</sup> where the pH value was assumed to be 3.0. The result of scaling shows that all the singlet states of RA and CAs can potentially inject electron to the conduction band of  $\text{TiO}_2$ . Most importantly, the  $T_1$  level is the closest to the CBE of  $\text{TiO}_2$  in RA5, and goes down systematically when  $n$  increases. The energy gap is in the region of  $1200-2600\text{ cm}^{-1}$  in RA5-CA8.

(2) *Empirical Analyses of Submicrosecond Time-Resolved Spectra.* To determine the mechanisms of charge recombination via the  $T_1$  state, we examined the rise and decay dynamics of the  $D_0^{+}$  and  $T_1$  absorptions (here, we will continue to use the word “absorptions” instead of “states”; the reason will be clarified later). Figure 8 shows a set of submicrosecond time-resolved absorption spectra of RA5, CA6, CA7, and CA8 bound to  $\text{TiO}_2$  nanoparticles in ethanol suspension; we focused our attention on those RA and CAs that exhibited the highest electron-injection efficiencies. All the RA and CAs exhibit the  $T_1$  and  $D_0^{+}$  absorptions, which can be characterized as

follows: (1) When  $n$  increases, the contribution of the  $T_1$  absorption decreases, whereas that of the  $D_0^{+}$  absorption increases. (2) In all the RA and CAs, the  $T_1$  absorption decays completely at longer delay times ( $100\text{ }\mu\text{s}$ ). (3) At the longer delay times, the  $D_0^{+}$  absorption is negligible in RA5, exhibits a certain indication in CA6, and increases in the order  $\text{CA7} < \text{CA8}$ . The apparent decay time profiles of the  $T_1$  and  $D_0^{+}$  absorptions were characterized as follows: (i) The  $T_1$  absorption exhibited a single-exponential decay with time constants, 19.6, 16.6, 9.5, and  $8.5\text{ }\mu\text{s}$  in RA5, CA6, CA7, and CA8, respectively. (ii) The  $D_0^{+}$  absorption exhibited biexponential decay with a pair of time constants, 0.9 and  $19.1\text{ }\mu\text{s}$  in RA5; 2.5 and  $57.4\text{ }\mu\text{s}$  in CA6; 1.9 and  $164\text{ }\mu\text{s}$  in CA7; and 2.5 and  $176\text{ }\mu\text{s}$  in CA8.

(3) *The SVD and Global-Fitting Analyses of Submicrosecond Time-Resolved Spectra.* We have built a model for the global fitting of the spectral-data matrixes based on the following considerations: (1) The analysis of the decay time profiles of the  $D_0^{+}$  absorption, mentioned above, strongly suggests the presence of at least two species giving rise to the same  $D_0^{+}$  absorption. A unique characteristic is the rapid decay of the transient absorption which took place within less than  $3\text{ }\mu\text{s}$ . (2) The SVD of the data matrixes showed the following values of  $V_1$ ,  $V_2$ ,  $V_3$ ,  $V_4$ , and  $V_5$  respectively: 15.6, 0.52, 0.40, 0.20, and 0.17 in RA5; 15.5, 0.58, 0.27, 0.18, and 0.16 in CA6; 8.4, 0.82, 0.59, 0.20, and 0.19 in CA7; and 5.3, 0.84, 0.40, 0.20, and 0.18 in CA8. In each case, the difference between the  $V_3$  and  $V_4$  values is definitely larger than that between the  $V_4$  and  $V_5$  values. Further, the basis spectra and the time profiles of the first three components showed clear physical meaning, but those of the rest of the components did not. The results rationalized to use a three-component analysis. (3) We built three different models: Model A, in which a sequential transformation of three components takes place eventually to the ground state; Model B, in which a common precursor splits into two different intermediates, and then both of them decay down to the ground state; and Model C, in which reversible transformations between the intermediates are added to Model B. In each model, we solved the rate equations for the relevant three components, and obtained the expressions for their populations as a sum of components that were to decay with a different set of time

**SCHEME 3: The Singlet and Triplet Energy Levels of RA and CAs Scaled to the CBE of  $\text{TiO}_2$  by the Use of One-Electron Oxidation Potentials**



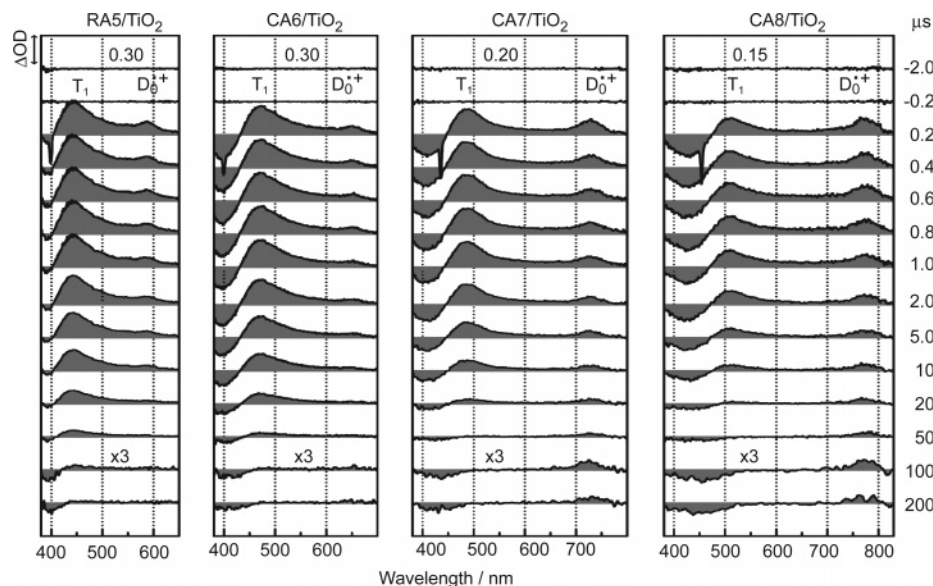


**Figure 8.** Submicrosecond time-resolved absorption spectra of RA and CAs bound to  $\text{TiO}_2$  nanoparticles in suspension. The ordinate scales of time-resolved spectra at 100 and 200  $\mu\text{s}$  are expanded by 3 times.

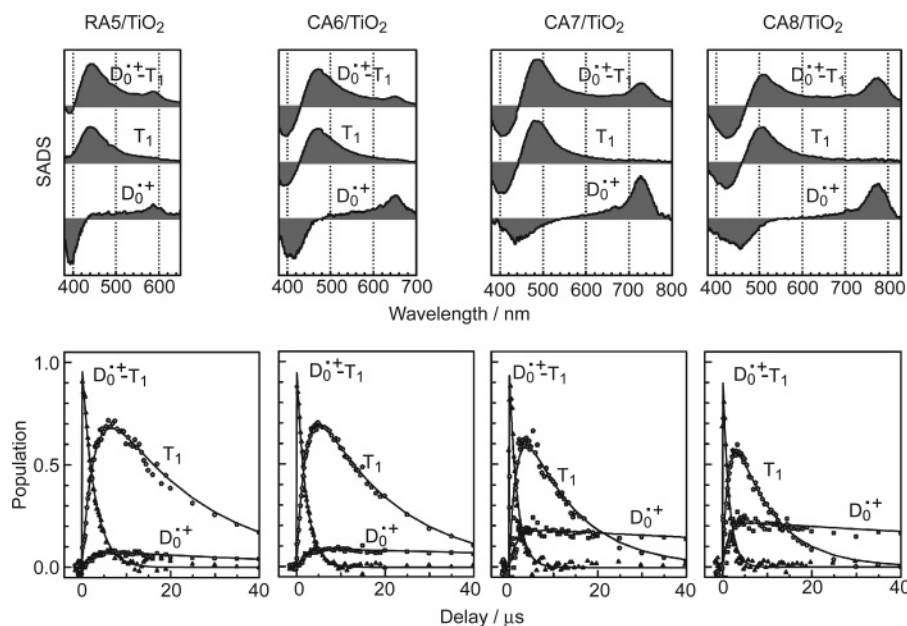


**Figure 9.** The results of the SVD and global-fitting analyses of submicrosecond time-resolved absorption spectra for RA and CAs bound to  $\text{TiO}_2$  nanoparticles in suspension: SADS (the upper panels) and time-dependent changes in population (the lower panels).

constants. The trials of global fitting, by the use of the three models, lead us to a conclusion that only Model B could fit the observed data matrixes of RA5, CA6, CA7, and CA8. Specifically, the model includes the generation of a  $\text{D}_0^{*+}\text{-T}_1$  complex (the common precursor) followed by transformation into the  $\text{D}_0^{*+}$  and the  $\text{T}_1$  states (the two different intermediates).

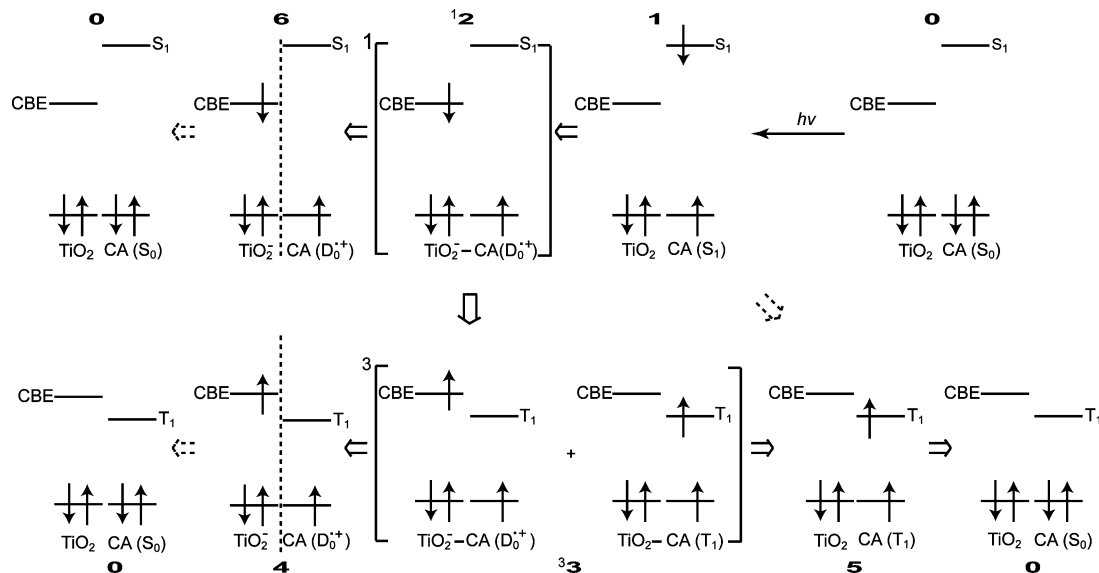
We will first present the results of SVD and global-fitting analysis, and then propose a possible mechanism:

(a) *The SADS Presenting a Set of Transient Species Involved.* Figure 9 (the upper panels) shows the SADS of the three relevant species, which can be assigned to (1) the  $\text{D}_0^{*+}\text{-T}_1$  complex, (2) the  $\text{T}_1$  state, and (3) the  $\text{D}_0^{*+}$  state. Those states can be clearly differentiated, by SADS, in terms of the  $\text{T}_1$  and  $\text{D}_0^{*+}$  transient absorptions and the bleaching of the ground-state absorption (abbreviated as “the  $\text{S}_0$  bleaching”). (1) The  $\text{D}_0^{*+}\text{-T}_1$  complex is characterized by a pair of  $\text{T}_1$  and  $\text{D}_0^{*+}$  absorptions and the  $\text{S}_0$  bleaching, (2) the  $\text{T}_1$  state is characterized by the  $\text{T}_1$  absorption and the  $\text{S}_0$  bleaching, and (3) the  $\text{D}_0^{*+}$  state is characterized by

the  $\text{D}_0^{*+}$  absorption and the  $\text{S}_0$  bleaching. (Now, we start introducing the words, “the  $\text{T}_1$  and  $\text{D}_0^{*+}$  states” and differentiate them from “the  $\text{T}_1$  and  $\text{D}_0^{*+}$  absorptions”.) The  $\text{S}_0$  bleachings in the former two species are shifted to the blue due to the overlap with the  $\text{T}_1$  absorption. All the  $\text{T}_1$  and  $\text{D}_0^{*+}$  transient absorption and the  $\text{S}_0$  bleaching systematically shift to the red in the order RA5, CA6, CA7, and CA8. In the  $\text{D}_0^{*+}\text{-T}_1$  complex, the relative intensity of the  $\text{T}_1$  absorption decreases, whereas that of the  $\text{D}_0^{*+}$  absorption increases in the same order.

(b) *The Time-Dependent Changes in Population and the Relevant Decay Time Constants of the Three Transient Species.* Figure 9 (the lower panels) shows the time-dependent changes in the population of the  $\text{D}_0^{*+}\text{-T}_1$  complex, the  $\text{T}_1$  state and the  $\text{D}_0^{*+}$  state in RA5, CA6, CA7, and CA8. The excited-state dynamics can be characterized as follows: (1) Basically the same excited-state dynamics is seen among all the RA and CAs examined; the decay of the  $\text{D}_0^{*+}\text{-T}_1$  complex accompanies the parallel rise of the  $\text{T}_1$  and  $\text{D}_0^{*+}$  states. (2) The contribution of

**SCHEME 4: Possible Pathways of Excitation, Transformation and Relaxation in the TiO<sub>2</sub>-CA Systems. Shown in Brackets Are the Charge-Separated States Having the Singlet and Triplet Characters, and Shown in Vertical Broken Lines Are the Long-Range Charge-Separated States.**



the  $T_1$  state decreases, whereas that of the  $D_0^{*+}$  state increases, in the order RA5, CA6, CA7, and CA8. (3) The decay of the  $D_0^{*+}$ - $T_1$  complex and that of the  $T_1$  state becomes faster in the same order, but the  $D_0^{*+}$  state does not decay in the time scale shown. {Table B in Supporting Information lists the time constants of the transformation from the  $D_0^{*+}$ - $T_1$  complex to the  $D_0^{*+}$  and the  $T_1$  states as well as the lifetimes of the  $D_0^{*+}$  and the  $T_1$  states. Those time constants can be affected by multiphoton excitation<sup>30</sup> (see the Experimental Section).}

(c) *A Possible Mechanism of Charge Recombination via the  $T_1$  State.* Scheme 4 exhibits all the possible transformations of the states of the TiO<sub>2</sub>-CA system after photoexcitation. In this scheme, each state is specified by the states of both TiO<sub>2</sub> and CA, but it can also be specified only by the states of CA, which can be probed by the present time-resolved absorption spectroscopy. By the use of this scheme, we are going to explain the excited-state dynamics, and then to propose a possible mechanism of transformation from the  $D_0^{*+}$ - $T_1$  complex to the  $D_0^{*+}$  and the  $T_1$  states.

First, we make the following four assumptions: (1) *Assumption 1.* The charge-separated state ( $^{12}$ ) is under the influence of strong interaction between the two components having the negative and positive charges. Therefore, it must be more stabilized energetically than neutral states, and can cause efficient spin-flip of the transferred electron due to the spin-orbit interaction. (Here, we specify the charge-separated state by the use of square brackets and spin multiplicity.) (2) *Assumption 2.* When the energies of a pair of states are similar to each other, as in the case of the charge-separated TiO<sub>2</sub><sup>-</sup>-CA( $D_0^{*+}$ ) state and the neutral TiO<sub>2</sub>-CA( $T_1$ ) state, "a charge-transfer complex" can be formed by its definitions ( $^{33}$ ). This can be described as a quantum-mechanical superposition of those two states. The most efficient mixing of those states is expected when the energy of the CBE of TiO<sub>2</sub> and that of the  $T_1$  state of CA are equal. (3) *Assumption 3.* The injected electron can migrate on the surface of the TiO<sub>2</sub> nanoparticles to a trapping site, leaving the radical cation  $D_0^{*+}$  of CA at the binding site. We indicate such a long-range charge-separated state by the use of a vertical broken line between the negative and the positive components (**6** and **4**). The trapped electron may come back to the binding site. (In the neutral states, we just align the

states of TiO<sub>2</sub> and CA side-by-side.) (4) *Assumption 4.* After photoexcitation, a sequence of exothermal transformations should take place according to the state ordering. However, it must be remembered that the excess energy deposited by photon on the excited state of CA needs to be dissipated during the transformation processes. Therefore, heat generated through the energy-dissipation processes can help to overcome barriers in the transformation from the charge-separated or the charge-transfer complex that are energetically stabilized.

Second, we try to trace the most likely pathway of transformations based in Scheme 4: When the CA molecule in the  $S_0$  state is excited to a singlet state by absorption of photon (**0** → **1**), the excited electron can be injected to the conduction band, and then, relaxed to the CBE of TiO<sub>2</sub> (**1** → **1<sup>2</sup>**). Then, the charge-separated state having a singlet character (**1<sup>2</sup>**) is formed. It can then transform to the charge-separated state having the triplet character (**3<sup>3</sup>**) due to the spin-orbit interaction (*Assumption 1*). When the CBE and  $T_1$  levels are located close-by, a charge-transfer complex (**3<sup>3</sup>**) can be formed consisting of the charge-separated state and the neutral state (*Assumption 2*). This charge-transfer complex can transform, by splitting of the two *potential* components, to the long-range charge-separated state (**3<sup>3</sup>** → **4**) and to the  $T_1$  state of CA bound to neutral TiO<sub>2</sub> (**3<sup>3</sup>** → **5**). In the former, the  $D_0^{*+}$  state (**4**) must take a long time for relaxation until the electron in the trapping site, on the surface of the TiO<sub>2</sub> nanoparticle, comes back to the CA binding site (*Assumption 3*), and neutralize the radical cation after spin flip (**4** → **0**). In the latter, the  $T_1$  state can decay in microseconds through the ordinary process of intersystem crossing (**5** → **0**).

Once the long-range charge-separated state having the triplet character (**4**) is formed, it may become difficult to return to the charge-transfer complex (**3<sup>3</sup>**), and then to transform to the  $T_1$  state (**5**) based on the following reasons: (1) The electron in the trapping site of TiO<sub>2</sub> nanoparticles needs to come back to the CA radical cation, (2) the spins of the pair of electrons on TiO<sub>2</sub> and the  $S_0$  state of the CA radical cation are parallel and repulsive, and (3) the **4** → **3<sup>3</sup>** → **5** transformation may need to overcome barriers. After a series of relaxation processes are over, and the dissipation of the excess energy is completed, there may be no heat energy available to overcome the barrier(s) (*Assumption 4*). Therefore, the direct transformation from the

$D_0^{*+}$  state (**4**) to the  $T_1$  state (**5**) is unlikely. This can be one of the reasons why we failed to detect this direct transformation.

On the other hand, the charge-separated state of the singlet character (**2**) may possibly decay to the ground state (**0**) within the particular state, or after proceeding to the long-range charge-separated state having a singlet character (**6**). However, due to the large energy gap between the CBE of  $TiO_2$  and the  $S_0$  state of CA (see Scheme 3), both processes must be much slower than the  $^1\mathbf{2} \rightarrow ^3\mathbf{3}$  transformation that is followed by the generation of the  $D_0^{*+}$  and  $T_1$  states, which actually took place within 10 ps (Figure 4). Therefore, the charge recombination directly to generate the  $S_0$  state is also unlikely. In the particular case of RA and CAs bound to  $TiO_2$  nanoparticles, the electron injection must finish quickly after saturating all the trapping sites on the surface of  $TiO_2$  nanoparticles. Then, the relaxation processes through the charge-transfer complex (**3**) will be greatly enhanced.

Finally, we further examine the above possible mechanism of charge recombination via the  $T_1$  state, referring to the results of the SVD and global-fitting analyses: We start with the charge-transfer complex consisting of the charge-separated  $TiO_2^- - CA(D_0^{*+})$  state and neutral  $TiO_2 - CA(T_1)$  state (**3**), which we simply call "the  $D_0^{*+} - T_1$  complex" in terms of the states of CA. Since resonance electron transfer takes place from the CBE of  $TiO_2$  to a higher vibrational level of the  $T_1$  state of CA (Assumption 2), the thermal energy that is generated during the processes of relaxation needs to be deposited on the  $T_1$  state (Assumption 4). Then, the contribution of the *potential*  $T_1$  state relative to that of the *potential*  $D_0^{*+}$  state, in the charge-transfer complex, is supposed to be determined by the energy gap between the CBE of  $TiO_2$  and the  $T_1$  level of CA. The smaller the energy gap, the larger the amount of the  $T_1$  state generated. Actually, the energy diagram in Scheme 3 shows that the energy gap increases in the order  $RA5 < CA6 < CA7 < CA8$ , while the SADS of the  $D_0^{*+} - T_1$  complex in Figure 7 (the upper panels) shows that the contribution of the *potential*  $T_1$  state relative to that of the *potential*  $D_0^{*+}$  state decreases in the order  $RA5 > CA6 > CA7 > CA8$ , in agreement with the above expectation.

Then, we proceed to the generation of the real  $T_1$  and  $D_0$  states: The time-dependent changes in population depicted in Figure 9 (the lower panels) show that the amount of the  $T_1$  state relative to the amount of the  $D_0^{*+}$  state, both generated from the  $D_0^{*+} - T_1$  complex, decreases in the order  $RA5 > CA6 > CA7 > CA8$ . In other words, the relative amounts of the *potential*  $T_1$  vs  $D_0^{*+}$  states in the  $D_0^{*+} - T_1$  complex are roughly proportional to the relative amounts of the real  $T_1$  vs  $D_0^{*+}$  states as the products.

The above observations strongly support the proposed mechanism of generating the  $T_1$  and  $D_0^{*+}$  states from the  $T_1 - D_0^{*+}$  complex ( $\mathbf{4} \leftarrow ^3\mathbf{3} \rightarrow \mathbf{5}$ ). The faster decay of the  $T_1$  state as well as the much slower decay of the  $D_0$  state can also be explained by the above-mentioned decay mechanisms of  $\mathbf{4} \rightarrow \mathbf{0}$  and  $\mathbf{5} \rightarrow \mathbf{0}$ . Thus, we propose a flow of events in Scheme 4, i.e.,  $^1\mathbf{2} \rightarrow ^3\mathbf{3} \rightarrow \mathbf{5}$ , as the mechanism of charge recombination via the  $T_1$  state.

## Discussion

**Comparison of the Present Results with Those of Other Investigators.** To reach the complete understanding of the mechanisms of electron injection and charge recombination, it is necessary to find out agreement and discrepancy, at the present stage, among the results and interpretations described here and those reported and proposed by other investigators.

(a) *Electron-Injection Mechanism.* Sundström and co-workers<sup>22</sup> examined CA9 bound to  $TiO_2$  nanoparticles in suspension,

and concluded as follows: When bound to  $TiO_2$ , the CA9 molecules inject electrons from the initially excited  $S_2$  ( $1B_u^+$ ) state into the conduction band of  $TiO_2$  with a quantum yield of 40%. No electron injection was seen from the  $S_1$  ( $2A_g^-$ ) state. The electron-injection pathways we proposed (Figure 7) do not contradict to their conclusion. The only difference is that the authors treated the  $1B_u^+$  and  $1B_u^-$  states collectively, whereas we treated them separately.

Weng and co-workers<sup>24</sup> examined RA5 bound to  $TiO_2$  nanoparticles. They assigned the  $S_3$ ,  $S_2$ , and  $S_1$  states of RA5 to the  $1B_u^+$ ,  $n\pi^*$ , and  $2A_g^-$  states, respectively, and concluded that electron injection takes place from the  $1B_u^+$  and  $n\pi^*$  states. On the other hand, we found only two singlet states, and assigned them to the  $1B_u^+$  and  $2A_g^-$  states, instead; we concluded that electron injection takes place from those two states. Since the SADS of their  $1B_u^+$  and  $n\pi^*$  states (Figure 3 of ref 24) are in general agreement with the SADS of our  $1B_u^+$  and  $2A_g^-$  states (Figure 5), the contradiction originates from the assignments proposed by the two groups. Here, we would like to mention that the above pair of SADS are similar to those of the  $1B_u^+$  and  $2A_g^-$  states of *all-trans*-retinal, and that the SADS of the  $n\pi^*$  state exhibits a completely different spectral pattern (see Figure 3 of ref 40). Further effort to identify the  $n\pi^*$  state in RA and CAs is necessary.

(b) *Charge Recombination Mechanism.* Weng and co-workers<sup>23</sup> found, in RA5 bound to  $TiO_2$  nanoparticles in ethanol suspension, the generation of the  $T_1$  state after charge-recombination. Sundström and co-workers<sup>22</sup> also found, in CA9 bound to  $TiO_2$  nanoparticles, that the radical cation recombines with the conduction band electron through two different channels: approximately one-half directly forms via the ground state, and the rest of it via the  $T_1$  state. Further, Weng and co-workers<sup>24</sup> showed, in RA5 bound to  $TiO_2$  nanoparticles, that charge recombination takes place mainly via the  $T_1$  state; they evaluated the branching ratio to be 6:1.

Both groups seem to consider that the  $D_0^{*+}$  state is the direct precursor of the  $T_1$  state. Initially, we also tried to analyze the time-resolved spectra assuming that the reverse electron transfer takes place from the CBE to the vacant  $T_1$  level of the  $D_0^{*+}$  state to form the  $T_1$  state. However, we failed to prove this mechanism by the SVD and global-fitting analyses. A successful SVD and global-fitting analysis led us to propose a new mechanism. Here, we would like to point out that the mechanism of triplet generation through the route  $^1\mathbf{2} \rightarrow ^3\mathbf{3} \rightarrow \mathbf{5} \rightarrow \mathbf{0}$  (see Scheme 4) can be regarded as a mechanism of photoprotection, when the electron injection to the trapping site of  $TiO_2$  ( $^1\mathbf{2} \rightarrow \mathbf{6}$ ) is saturated, as first proposed by Weng and co-workers<sup>23</sup> and as we described in the Introduction section of the following article.<sup>21</sup>

Concerning the electron-injection mechanism, all three research groups will hopefully reach the same conclusion, when the assignment of the singlet states is established. However, further investigation is absolutely necessary to establish the mechanism of charge recombination. Time-resolved absorption spectroscopy in all the time range from the subpicosecond to millisecond as well as the SVD and global-fitting analyses of the time-resolved spectral-data matrixes obtained will solve this issue.

**The Conjugation-Length Dependence of Electron Injection and Charge Recombination: Correlation with the Performance of DSSCs.** Now, we are going to summarize the results concerning the dependence of electron injection and charge recombination on  $n$  in RA and CAs bound to  $TiO_2$  nanoparticles, and correlate them with the conversion efficiency



and the IPCE at 420 nm of DSSCs answering the questions addressed in the Introduction section.

(1) How do the electron-injection pathway and efficiency depend on  $n$ ? In the present investigation, we have examined a set of RA and CAs having the number of conjugated double bonds ( $n$ ) 5, 6, 7, 8, 9, and 11, whose singlet and triplet levels were characterized by extrapolation of those levels determined in Cars,  $n = 9$ –13. The initial excited-state dynamics in the subpicosecond-to-picosecond time range, for RA and CAs free and bound to  $\text{TiO}_2$ , well reflected the state ordering shown in the energy diagram. It was found that RA5, CA6, CA7, and CA8 have two channels of electron injection ( $1\text{B}_\text{u}^+$  and  $2\text{A}_\text{g}^-$ ), whereas CA9 and CA11 have a single channel ( $1\text{B}_\text{u}^+$ ). The time constants of internal conversion and electron injection, which were determined by the SVD and global-fitting analyses, allowed us to evaluate the electron-injection efficiencies as shown in Table 1: RA5 and CA6 92%, CA7 98%, CA8 94%, CA9 60%, and CA11 29%.

(2) How does the charge recombination via the  $\text{T}_1$  state depend on  $n$ ? To examine charge recombination via the  $\text{T}_1$  state, we determined the one-electron oxidation potentials of RA and CAs, and scaled their singlet and triplet levels to the CBE of  $\text{TiO}_2$ . The  $\text{T}_1$  level of RA5 was lower but the closest to the CBE, and those of CAs systematically decreased when  $n$  increased. Then, we examined the excited-state dynamics of the  $\text{D}_0^{*+}$  and  $\text{T}_1$  states in the submicrosecond-to-hundred microsecond time range. The SVD and global-fitting analyses of the time-resolved spectra lead us to a new scheme of triplet generation, in which the  $\text{D}_0^{*+}$ – $\text{T}_1$  complex is formed first, and then it splits into the  $\text{D}_0^{*+}$  and  $\text{T}_1$  states. The partition ratio was calculated by the use of the decay time constants determined by the SVD and global-fitting analyses. The partition ratio to the  $\text{T}_1$  state decreased in the order RA5 (92%) > CA6 (89%) > CA7 (82%) > CA8 (75%). [See Table B in the Supporting Information.]

(3) How does the dependence on  $n$  correlate with that of the conversion efficiency and the IPCE when DSSCs are fabricated by the use of the  $\text{TiO}_2$ –RA and  $\text{TiO}_2$ –CA systems? As shown in Figure 1, both the conversion efficiency and the IPCE at 420 nm exhibit the maximum in CA7, and they decrease on both sides toward RA5 and CA11. The electron-injection efficiency of RA and CAs bound to the  $\text{TiO}_2$  nanoparticles (Figure 1c) also exhibited the maxima in CA7, and it decreased systematically toward CA11. Close correlation is found among the three parameters in the region of CA7–CA11 (much closer correlation is found to the IPCE at 420 nm rather than in the conversion efficiency). However, the electron-injection efficiency does not decrease so clearly toward RA5. When we regard the generation of the  $\text{T}_1$  state as a leaking channel, whereas the generation of the  $\text{D}_0^{*+}$  state is regarded as an active channel in electron injection, the decrease in the conversion efficiency and the IPCE at 420 nm toward RA5 can be nicely explained.

**Acknowledgment.** The authors would like to thank Dr. Yuxiang Weng for reading the manuscript and making comments. They are also grateful to Mr. Toshinobu Fujii (Hokuto Denko, Japan) for the construction of the spectroelectrochemical cell, and Dr. Hansgeorg Ernst, BASF, for providing CE9 and CE11. This work has been supported by a grant from Hyogo Science and Technology Association, a grant from NEDO (New Energy and Industrial Technology Development Organization, International Joint Research Grant), and a grant from the Ministry of Education, Culture, Sports, Science and Technology for an Open Research Center Project “The Research Center of Photo-Energy Conversion”.

**Supporting Information Available:** Listing of absorption peaks and time constants. This material is available free of charge via the Internet at <http://pubs.acs.org>.

## References and Notes

- O'Regan, B.; Grätzel, M. *Nature* **1991**, *353*, 737.
- Hagfeldt, A.; Grätzel, M. *Chem. Rev.* **1995**, *95*, 49.
- Kalyanasundaram, K.; Grätzel, M. *Coord. Chem. Rev.* **1998**, *77*, 347.
- Grätzel, M. *J. Photochem. Photobiol. A: Chem.* **2004**, *164*, 3.
- Tachibana, Y.; Moser, J. E.; Grätzel, M.; Klug, D. R.; Durrant, J. R. *J. Phys. Chem.* **1996**, *100*, 20056.
- Ellingson, R. J.; Asbury, J. B.; Ferrere, S.; Ghosh, H. N.; Sprague, J. R.; Lian, T.; Nozik, A. J. *J. Phys. Chem. B* **1998**, *102*, 6455.
- Asbury, J. B.; Ellingson, R. J.; Ghosh, H. N.; Ferrere, S.; Nozik, A. J.; Lian, T. *J. Phys. Chem. B* **1999**, *103*, 3110.
- Asbury, J. B.; Hao, E.; Wang, Y.; Ghosh, H. N.; Lian, T. *J. Phys. Chem. B* **2001**, *105*, 4545.
- Benkö, G.; Kallioinen, J.; Korppi-Tommola, J. E. I.; Yartsev, A. P.; Sundström, V. *J. Am. Chem. Soc.* **2002**, *124*, 489.
- Asbury, J. B.; Anderson, N. A.; Hao, E.; Ai, X.; Lian, T. *J. Phys. Chem. B* **2003**, *107*, 7376.
- Hara, K.; Tachibana, Y.; Ohga, Y.; Shinpo, A.; Suga, S.; Sayama, K.; Sugihara, H.; Arakawa, H. *Sol. Energy Mater. Sol. Cells* **2003**, *77*, 89.
- Kitamura, T.; Ikeda, M.; Shigaki, K.; Inoue, T.; Anderson, N. A.; Ai, X.; Lian, T.; Yanagida, S. *Chem. Mater.* **2004**, *16*, 1806.
- Horiuchi, T.; Miura, H.; Sumioka, K.; Uchida, S. *J. Am. Chem. Soc.* **2004**, *126*, 12218.
- Sashima, T.; Nagae, H.; Kuki, M.; Koyama, Y. *Chem. Phys. Lett.* **1999**, *299*, 187.
- Sashima, T.; Koyama, Y.; Yamada, T.; Hashimoto, H. *J. Phys. Chem. B* **2000**, *104*, 5011.
- Furuichi, K.; Sashima, T.; Koyama, Y. *Chem. Phys. Lett.* **2002**, *356*, 547.
- Koyama, Y.; Rondonuwu, F. S.; Fujii, R.; Watanabe, Y. *Biopolymers* **2004**, *74*, 2.
- Rondonuwu, F. S.; Yokoyama, K.; Fujii, R.; Koyama, Y.; Cogdell, R. J.; Watanabe, Y. *Chem. Phys. Lett.* **2004**, *390*, 314.
- Akahane, J.; Rondonuwu, F. S.; Fiedor, L.; Watanabe, Y.; Koyama, Y. *Chem. Phys. Lett.* **2004**, *393*, 184.
- Gao, F. G.; Bard, A. J.; Kispert, L. D. *J. Photochem. Photobiol. A: Chem.* **2000**, *130*, 49.
- Wang, X.-F.; Fujii, R.; Ito, S.; Koyama, Y.; Yamano, Y.; Ito, M.; Kitamura, T.; Yanagida, S. *Chem. Phys. Lett.*, submitted for publication.
- Pan, J.; Benkö, G.; Xu, Y.; Pascher, T.; Sun, L.; Sundström, V.; Polívka, T. *J. Am. Chem. Soc.* **2002**, *124*, 13949.
- Weng, Y.-X.; Li, L.; Liu, Y.; Wang, L.; Yang, G.-Z.; Sheng, J.-Q. *Chem. Phys. Lett.* **2002**, *355*, 294.
- Zhang, L.; Yang, J.; Wang, L.; Yang, G.-Z.; Weng, Y.-X. *J. Phys. Chem. B* **2003**, *107*, 13668.
- Zhang, J.-P.; Fujii, R.; Qian, P.; Inaba, T.; Mizoguchi, T.; Koyama, Y.; Onaka, K.; Watanabe, Y.; Nagae, H. *J. Phys. Chem. B* **2000**, *104*, 3683.
- Fujii, R.; Inaba, T.; Watanabe, Y.; Koyama, Y.; Zhang, J.-P. *Chem. Phys. Lett.* **2003**, *369*, 165.
- Zhang, J.-P.; Inaba, T.; Watanabe, Y.; Koyama, Y. *Chem. Phys. Lett.* **2000**, *331*, 154.
- Fujii, R.; Koyama, Y.; Mortensen, A.; Skibsted, L. H. *Chem. Phys. Lett.* **2000**, *326*, 33.
- Britton, G. UV-Visible spectroscopy. In *Carotenoids. Vol. 1B: Spectroscopy*; Britton, G., Liaaen-Jensen, S., Pfander, H., Eds.; Birkhäuser Verlag: Basel, Switzerland, 1995; Chapter 2, pp 57.
- Haue, S. A.; Tachibana, Y.; Willis, R. L.; Moser, J. E.; Grätzel, M.; Klug, D. R.; Durrant, J. R. *J. Phys. Chem. B* **2000**, *104*, 538.
- Katoh, R.; Furube, A.; Hara, K.; Murata, S.; Sugihara, H.; Arakawa, H.; Tachiya, M. *J. Phys. Chem. B* **2002**, *106*, 12957.
- Tavan, P.; Schulten, K. *J. Chem. Phys.* **1986**, *85*, 6602.
- Pariser, R. *J. Chem. Phys.* **1956**, *24*, 250.
- Callis, P. R.; Scott, T. W.; Albrecht, A. C. *J. Chem. Phys.* **1983**, *78*, 16.
- Englman, R.; Jortner, J. *Mol. Phys.* **1970**, *18*, 145.
- Rondonuwu, F. S.; Watanabe, Y.; Fujii, R.; Koyama, Y. *Chem. Phys. Lett.* **2003**, *376*, 292.
- Tavan, P.; Schulten, K. *Phys. Rev. B* **1987**, *36*, 4337.
- Rondonuwu, F. S.; Taguchi, T.; Fujii, R.; Yokoyama, K.; Koyama, Y.; Watanabe, Y. *Chem. Phys. Lett.* **2004**, *384*, 364.
- Duonghong, D.; Ramsden, J.; Grätzel, M. *J. Am. Chem. Soc.* **1982**, *104*, 2977.
- Yamaguchi, S.; Hamaguchi, H. *J. Chem. Phys.* **1998**, *109*, 1397.